

Flow properties of sandstone and carbonate rocks by X-ray computed tomography

T. R. Zakirov*, A. A. Galeev, E. A. Korolev and E. O. Statsenko

Kazan Federal University, Kazan, 4/5 Kremlyovskaya Str, 420008, Russia

We report the use of X-ray micro-CT and numerical simulations for studying the reservoir properties of sandstone and carbonate rocks in the Melekes depression of the Volga-Ural antecline, Russia. To simulate the flow of a viscous fluid in the pore scale, we use a mathematical model which consists of the continuity equation, stationary Navier–Stokes equations and Darcy law. As a result of computational micro-scale experiments on digital three-dimensional images of sandstone, we get satisfactory compatible permeability coefficients, which are calculated using Navier–Stokes and Kozeny–Carman equations. Carbonates with fracture porosity reveals significant variations in permeability coefficients, calculated by the two methods. The Kozeny–Carman equation can describe the flow properties of carbonates with a predominantly matrix porosity. It is shown that a pronounced heterogeneity of the pore space leads to the representative elementary volume for permeability coefficient in carbonates several times larger than in sandstones.

Keywords: Carbonate, flow properties, permeability, sandstone, X-ray computed tomography.

THE ability of porous media to transmit fluids is described by the absolute permeability coefficient representing a macroscopic parameter of continuum mechanics on the basis of the Darcy's law^{1,2}. To estimate the absolute permeability coefficient on a model of the microscopic pore space, the Kozeny–Carman equations were used to take into account the complex structure of the flow channels in real porous media^{3–6}.

Electron microscopy and X-ray computed tomography (CT) along with computational tools have been used for the digital three-dimensional imaging of porous media with submicron and nanometre geometrical resolution^{7–14}. X-ray micro-CT technique provides a three-dimensional digital image of the porous body at a resolution of a few micrometres, which is sufficient to study the pore space in dominating oil reservoirs rocks, such as carbonates and sandstones.

For analysis of the three-dimensional geometry of the pore structure modelling the process of fluid flow in the pore scale and evaluation of absolute permeability coefficients, we used digital tomographic images of the internal

structure of sandstone and carbonate oil reservoirs. The aim of the present study is to look the solution of the direct problem of estimating permeability based on microscopic pore structures for laminar flow without capillary interactions.

The samples were oil-bearing sandstones and carbonates of Permian and Carboniferous age of the Melekes depression of the Volga-Ural antecline, Russia.

The composition of sandstone is polymineral, slightly calcareous, unevenly oil-saturated, having a fine- to medium-grained structure and locally observed silt. Visually, rocks are characterized by greenish-grey colour, with numerous dark-brown spots of oil effusion, which cause their mottled texture.

According to petrographic analysis, sandstones comprise 85–90% mineral and rock grains along with 10–15% cementing material. The allogenic component of the average size of 0.25–0.5 mm is constituted by poorly-rounded elongated quartz grains and well-rounded isometric rubble of siliceous rocks, and to a lesser degree by angular grains of feldspar and rare flakes of chlorite and muscovite. Detrital material forms a dense structural packing in the volume of the sand bed. Fragments of minerals and rocks contact by convex and tapered surface portions, forming a point contact type. In fixed rock there are rare areas containing regenerated fragments of quartz, forming cluster aggregates with convex–concave (conformal) contact fit. Detrital material is cemented by calcite cement. Pore filling cement is partially dissolved.

Carbonates are bioclastic zoomorphic, sulphated and, to varying degrees, oil-saturated limestones and dolomites. Visually, they are dark-brown rocks with veinlets and clustered anhydrite segregations. Often they are whipped by subvertical fissures filled by gypsum–anhydrite aggregation.

According to the petrographic analysis, carbonates comprise 80–85% organic residues and 15–20% cementing material. Fossils sizes of 0.25–1.0 mm are represented mainly by integral tests of foraminifera, and to a lesser extent by fragments of brachiopod sections, crinoid segments, calcified algae and rare corals. Carbonate cement is unevenly leached. Consequently, there is irregular arrangement of compact and decompressed sections of varying thickness and length in the rocks. The pores are mostly of interskeletal type, 0.05–0.25 mm in diameter; the communicating throats which permeate the rock in all directions are oil-filled.

Core plugs were measured using a micro- and nanofocus system for 3D CT (GE Phoenix v|tome|x s). All measurements were carried out using a nanofocus X-ray tube at 120 kV voltage and a 90 mA current. The preliminary computer processing, segmentation and analysis of the geometric characteristics of the tomograms were performed using the Avizo Fire Edition software (Visualization Sciences Group). The methods and techniques of segmentation of micro-CT images are reviewed elsewhere¹⁵.

*For correspondence. (e-mail: tirzakirov@kpfu.ru)

Figure 1 *a* shows a fragment of the original CT image, taken at a resolution of 10 μm , in which black corresponds to areas with the lowest X-ray attenuation coefficient and the lighter shades of grey correspond to areas with higher X-ray attenuation coefficient. Figure 1 *b* shows the same fragment of the sample after the procedure of image division (segmentation) into two phases (pores and skeleton). The digital array corresponding to the segmented image can be represented as a file with the voxels coordinates (x, y, z) and '0' for pores and '1' for skeleton.

The results of image processing used in the analysis of the porous structures of the core plugs were used to set the boundary conditions on the solid phase in the modelling of flow.

The flow of the fluid in the pore space can be represented through the motion of an incompressible viscous fluid. For a description of this type of flow, we use the continuity equation (i.e. eq. (1)) and the Navier–Stokes equations (i.e. eqs (2)–(4))¹⁶. The adoption of the stationary fluid flow based on the results of Mostaghimi *et al.*⁶ shows that the flow rate at low differential pressures (a few kPa) is very small (tens of mm/s). Consequently, the inertial forces in comparison with the diffusion forces can be disregarded for the problem being solved.

$$\frac{\partial u}{\partial x} + \frac{\partial v}{\partial y} + \frac{\partial w}{\partial z} = 0, \quad (1)$$

$$\mu \left(\frac{\partial^2 u}{\partial x^2} + \frac{\partial^2 u}{\partial y^2} + \frac{\partial^2 u}{\partial z^2} \right) = \frac{1}{\rho} \frac{\partial P}{\partial x}, \quad (2)$$

$$\mu \left(\frac{\partial^2 v}{\partial x^2} + \frac{\partial^2 v}{\partial y^2} + \frac{\partial^2 v}{\partial z^2} \right) = \frac{1}{\rho} \frac{\partial P}{\partial y}, \quad (3)$$

$$\mu \left(\frac{\partial^2 w}{\partial x^2} + \frac{\partial^2 w}{\partial y^2} + \frac{\partial^2 w}{\partial z^2} \right) = \frac{1}{\rho} \frac{\partial P}{\partial z}, \quad (4)$$

where P is the pressure field, (u, v, w) the velocity field, ρ the density of the liquid and μ is the fluid viscosity. Pressure and speed in the formulation of the problem are functions that depend on the cell coordinates in the digital image of the core plug.

The use of the eqs (1) and (2) to describe the motion of a fluid in porous media is different from the approach discussed in the literature^{17–19}, where the fluid flow is described by the continuity equations in which the coefficients of porosity and permeability are averaged in terms of their values.

As a structural unit of the computational grid, we chose a cubic cell corresponding to one voxel. The spatial dimension of voxels corresponds to resolution of micro-CT image.

For discretization of eqs (1) and (2), the finite difference method is used^{20,21}. For the formation of the grid, we used the 'method of markers and cells' (MAC)^{1,22,23}. The structure of the cell in the MAC method is designed so that the pressure $P_{i,j,k}$ is defined at the centre, and the velocity components, e.g. $u_{i-1/2,j,k}$ and $u_{i+1/2,j,k}$, are found in the centre of its left and right faces respectively. The solution of the resulting discretized matrix equation is computed in the SPARSKIT package²⁴. For solving the nonsymmetrical equation system, we use the biconjugate gradient stabilized method (BCGSTAB) and generalized minimal residual method (GMRES) on Krylov subspace²⁵. The convergence criteria of solution is 10^{-4} . To accelerate the solution of the system, we use LU-factorization of matrix (the module ILUT), where the initial matrix representation is a composition of two matrices L and U , where L is the lower triangular matrix and U the upper triangular matrix.

The external boundaries and solid surfaces within the computational domain conditions were applied with respect to liquid impermeability and adhesion²³. These conditions indicate that velocity components which are normal and tangential to the outer faces equate to zero, while on the internal solid surfaces they are described as follows. For example, if the cell number (i, j, k) refers to a solid phase, the velocity components $u_{i-1/2,j,k}$, $u_{i+1/2,j,k}$, $v_{i,j-1/2,k}$, $v_{i,j+1/2,k}$, $w_{i,j,k-1/2}$ and $w_{i,j,k+1/2}$ equate to zero.

The model for the fluid adopted the following parameters: viscosity $\mu = 1.5 \times 10^{-6} \text{ M}^2/\text{C}$ (1.5 cPs) and density $\rho = 1000 \text{ kg/m}^3$.

Computational experiments were carried out on cubic fragments of the digital core plug with linear dimensions of 25–200 voxels, which were segmented and cut from CT images. In general, the absolute permeability has a tensor property. The full analysis of the symmetrical tensor of rank two requires determination of all the diagonal and off-diagonal components, their principal axes and principal values. This procedure and analysis of tensor requires special consideration. From a practical point of view for simulation of fluid flow within sedimentological layers, we chose the pressure drop on opposite faces of

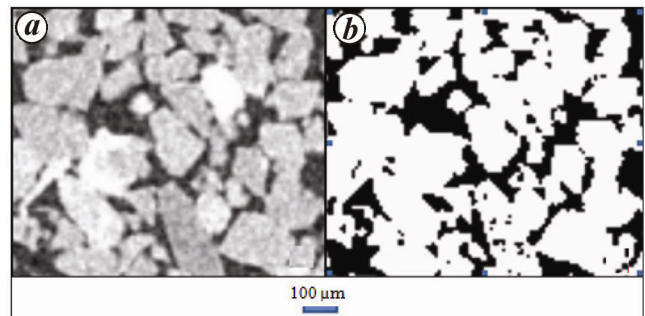


Figure 1. Virtual cross-section of sandstone CT image. *a*, Original image; *b*, Image after segmentation.

the cube along the x -axis in the plane orthogonal to the z -axis of the vertical well.

As a structural unit of the computational grid, we chose a cubic cell corresponding to one voxel. On the front face of the cube, the pressure P_{in} was 1.1 kPa, and on the opposite face it was $-P_{out} = 0.1$ kPa. We modelled experimental conditions with constant pressure drop, which are commonly used, e.g. Mostaghimi *et al.*⁶. As a numerical parameter describing the flow characteristics of porous media received, k_x represents the component of absolute permeability tensor. The value k_x is calculated on the basis of solving the system of equation, i.e. eqs (1) and (2) with given boundary conditions, based on the following equation¹

$$k_x = \frac{\left(\sum_{\beta} u_{\beta} dS_{\beta} \right) \cdot \rho \mu}{\left(\sum_{\beta} dS_{\beta} \right) \cdot \text{grad}(P)}, \quad (5)$$

where dS indicates cell area facing the outlet section, and the index β – cell number indicates the output section.

The proposed mathematical model and corresponding software code have been tested for problems with known analytical solutions, such as the Couette and the Poiseuille flows¹⁶. The relative error in the comparison of calculation results did not exceed 5%. Moreover, tests were conducted on the numerical models of the following porous media: sandstone 1(S1), sandstone 3(S3), sandstone 5(S5), sandpack (F42B), carbonate (C1) and carbonate (C2) from the open digital core plugs library of Imperial College London²⁶. The permeability coefficients obtained on the basis of our computational experiments showed satisfactory agreement with the known flow characteristics of samples with a relative error not greater than 7%.

Figures 2 *a* and 3 *a* show the structure of the pore space $200 \times 200 \times 200$ voxels for sandstone and carbonate at a resolution of 10 and 12.7 μm respectively. For visualization of fluid flow, we built velocity fields in sandstone Ss15 (Figure 2 *b*) and carbonate Cb5 (Figure 3 *b*), which were normalized by the maximum values. The results of computational experiments reveal the structure of the flow. Figures 2 *b* and 3 *b* show that in the above sandstone sample the fluid flow is uniformly distributed throughout the volume of the core plug and that it also occurs in fine pores (20–30 μm), while fluid flow in carbonate is more heterogeneous and occurs mainly in the major channels (i.e. those that exceed 100 μm respectively). The most common approach for calculating the permeability of porous media is the Kozeny–Carman capillary model³. According to this method, the porosity coefficient m and specific pore surface area S_V have the following relationship^{3,5,6}

$$k_{\text{Carman}} = \frac{m^3}{c S_V^2}. \quad (6)$$

In eq. (6), the parameter S_V is calculated as the ratio of the surface area of pores to the volume of the sample; coefficient c , called the Carman constant, is represented as the product of two quantities: $c = \gamma \times \varphi^2$, where γ characterizes the cross-sectional shape of the channel, and represents pore tortuosity. Romm³ has described the results of experimental studies in which the parameter c has been calculated from eq. (6) for artificial porous

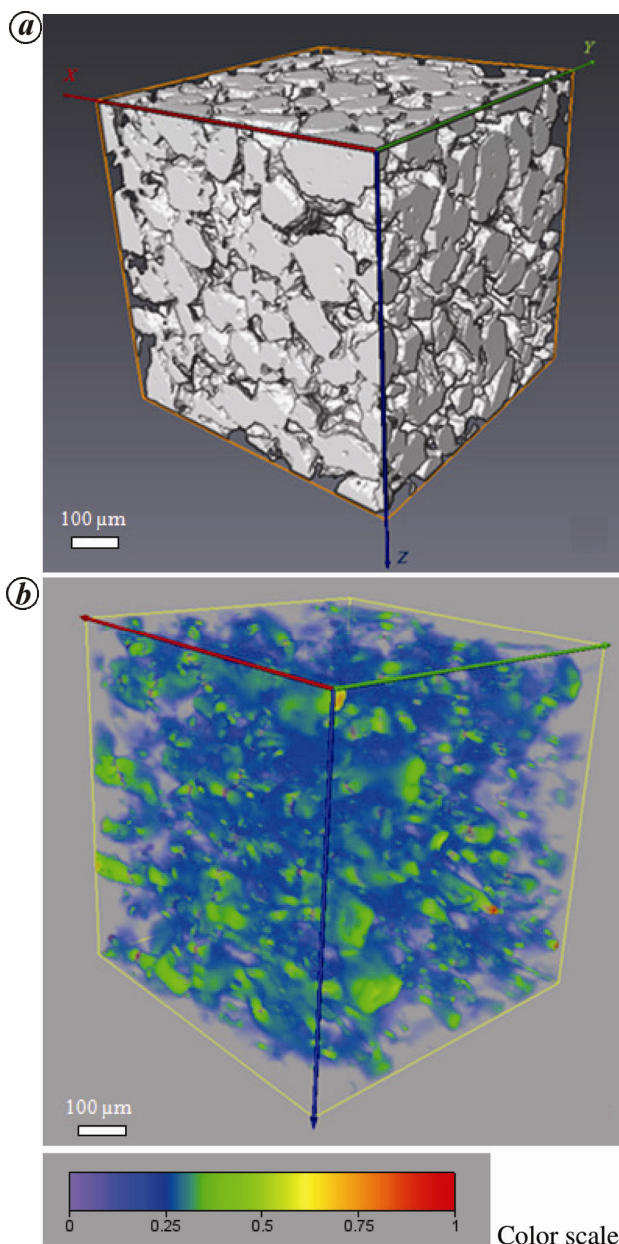


Figure 2. Results of computational experiments. *a*, Porous structure of sandstone Ss15. *b*, Velocity field of the fluid in the pores (with colour scale showing the normalized value of velocity).

media with different types of channel cross-sections (circle, ellipse, rectangle, etc.)

$$c = \frac{m^3}{k_{\text{Exp}} S_V^2}. \quad (7)$$

Experiments have shown that the value of c varies in the range 4.7–6.0 (ref. 3). The numerical value of c can also be estimated on the basis of the solution of the Navier–Stokes equations^{1–4}

$$c = \frac{m^3}{k_{\text{NS}} S_V^2}. \quad (8)$$

Table 1 shows the flow characteristics estimated on the basis of digital models from segmented tomographic images of sandstone. Permeability coefficients (column 5, Table 1) were calculated using the Kozeny–Carman equation⁶ at $c = 5$.

As seen in Table 1 (column 7), the Carman constant calculated using eq. (6) is in the range (4.0–8.3), which is slightly wider than the interval (4.7–6.0) for sandstone^{3,6}. According to eq. (8), the c variation range (4.0–8.3) for SS1 corresponds to k_{Carman} variation range (6.17–12.82) of absolute permeability coefficients. Nevertheless, it may be noted that sandstones have satisfactory compatible permeability coefficients, which are calculated using two different methods (Table 1, column 6). The difference in the porosity coefficients estimated from the tomographic images with different segmentation procedures does not exceed 7% (ref. 15).

Table 2 shows the flow characteristics of carbonate rocks. Carbonates are characterized by significant variations in the permeability coefficients calculated using eqs (3) and (4) (Table 2, column 6), and values of the Carman constant (Table 2, column 7), being far beyond the range (4.7–6.0) given in Romm³. Such discrepancies in the numerical values during the calculation of carbonate flow characteristics using the two methods were also observed by Mostaghimi *et al.*⁶.

Figure 4 shows the virtual sections of digital models of sandstone Ss15 and carbonate Cb5, as scanned at a resolution of 10.0 μm and 18.4 μm respectively. Comparison of the two images in Figure 4 shows that the carbonate rock of the studied section, unlike the sandstone, has a strongly inhomogeneous structure.

Figures 5 and 6 show graphs describing the porosity changes of the samples along the x -axis (direction of the applied pressure drop) for sandstone and carbonate respectively. The thickness of the slice is 10 voxels. As seen in Figure 5, sandstones have uniform distribution of porosity, in which the difference between the highest and lowest values of the porosity coefficients does not exceed 10%. The porosity distribution curve (Figure 6) of the

carbonate samples has a stick-slip characteristic, and the difference between the minimum and maximum values exceeds 100%: for sample Cb2, this parameter ranges from 0.09 to 0.17; for Cb3 from 0.04 to 0.14, and for Cb6, from 0.06 to 0.18. Such behaviour is a consequence of the strong heterogeneity of the pore and channel structure, which controls the flow properties.

We restrict our consideration to laboratory-scale (pore and core scales) procedures which need upscaling of physical properties from highly heterogeneous microscopic pore scale (flow in pores) to the macroscopic scale approximating continuum (Darcy flow), and which assume the estimation of representative elementary volume (REV)^{27,28}. Essentially, REV is the smallest volume of the sample which can be considered as homogeneous, so its flow characteristics are representative for the rock as a whole. The REV value is estimated using an

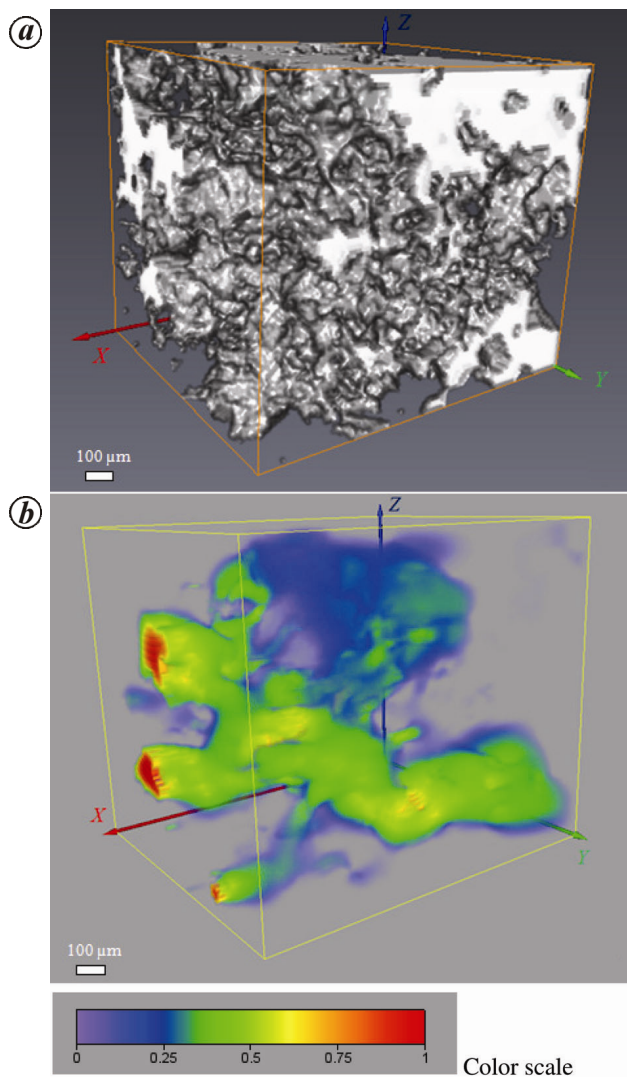


Figure 3. Results of computational experiments. *a*, Porous structure of carbonate Cb5. *b*, Velocity field of the fluid in the pores (with colour scale showing the normalized value of velocity).

Table 1. Reservoir properties of sandstones calculated from X-ray CT images

Sample	Porosity m relative units	Specific pore surface S_v (mm^{-1})	Permeability coefficient k_{NS} (μm^2)	Permeability coefficient of Carman k_{Carman} (μm^2)	Fractional deviation $d =$ $100 \cdot (k_{NS} - k_{Carman}) / k_{NS}$ (%)	Carman constant calculated using eq. (6)
Ss1	0.354	29.41	11.62	10.25	11.8	4.4
Ss2	0.392	15.86	28.88	47.89	-65.8	8.3
Ss3	0.353	12.56	37.545	55.76	-48.5	7.4
Ss4	0.442	16.58	40.44	62.82	-55.3	7.8
Ss5	0.433	15.66	49.15	66.2	-34.7	6.7
Ss6	0.383	14.73	39.58	51.79	-30.8	6.5
Ss7	0.462	12.42	98.15	127.85	-30.3	6.5
Ss8	0.490	12.76	100.29	144.51	-44.1	7.2
Ss9	0.553	12.44	274.26	218.55	20.3	4.0
Ss10	0.493	13.08	111.83	140.07	-25.3	6.3
Ss11	0.503	12.98	124.63	151.07	-21.2	6.1
Ss12	0.444	11.85	76.74	124.66	-62.4	8.1
Ss13	0.404	41.83	7.29	7.53	-3.3	5.2
Ss14	0.451	11.49	122.71	138.66	-13.0	5.7
Ss15	0.482	18.54	56.93	65.15	-14.4	5.7

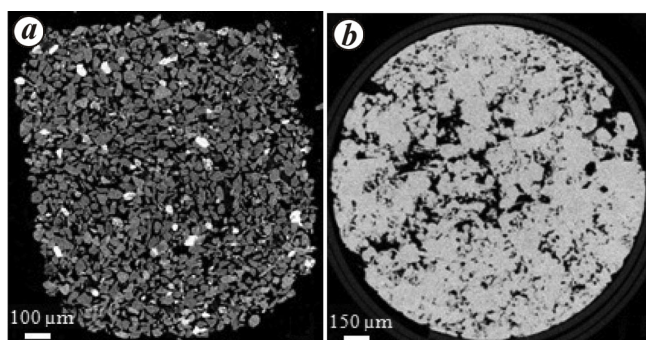


Figure 4. Virtual sections of CT images. *a*, Sandstone Ss15; *b*, Carbonate Cb5.

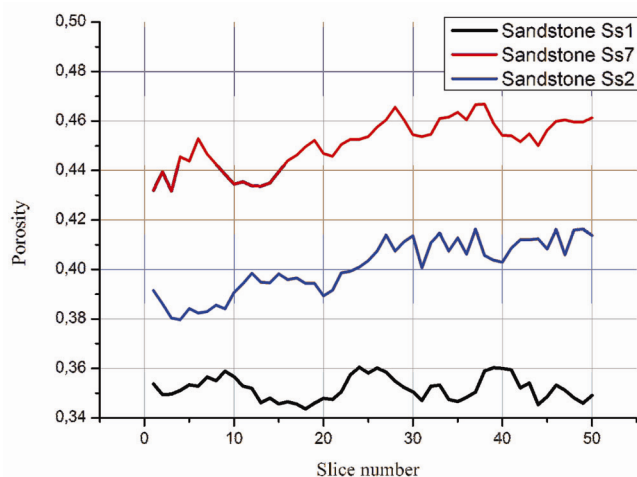


Figure 5. Distribution of porosity on virtual sections of CT images for sandstone.

iterative process in which the variation of flow characteristics, that can be achieved by successively increasing the sample volume, becomes negligible.

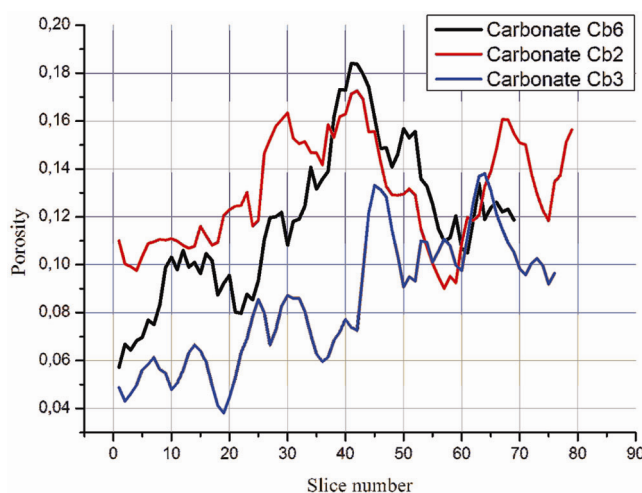
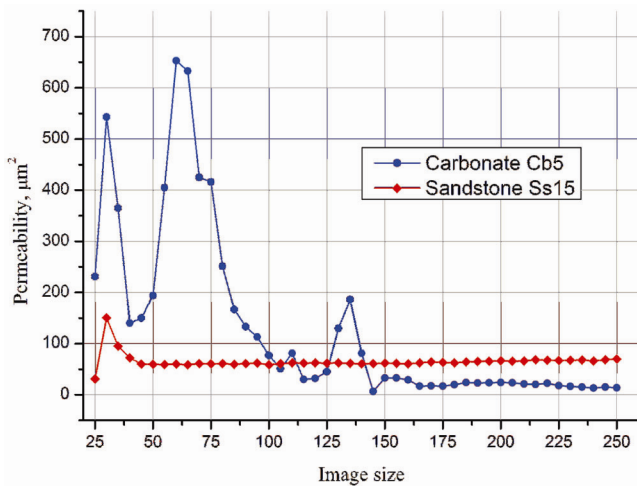


Figure 6. Distribution of porosity on virtual sections of CT images for carbonate.

Figure 7 shows a graph of permeability coefficients calculated using eqs (1)–(3) from X-ray CT images of sandstone Ss15 and carbonate Cb5, at successive increased modelling volume. Based on Figure 7, we conclude that insignificant change in the value of the permeability coefficient for sandstone is observed for volumes larger than 50 voxels (or 0.76 mm). Thus, the size of REV for the sandstone is 0.76 mm³. Another characteristic of the curve in Figure 7 is observed for carbonate due to the more pronounced heterogeneity of the pore space (Figure 6). It should be mentioned that carbonate pore space is represented by two distinct porosities: ‘matrix’ and ‘fractures’⁵. At submicron scale a single, occasionally occurring fracture of high permeability can predetermine the flow characteristics of considered volume (Table 2, Figure 7). We performed additional calculation using eqs (5) and (6) on the fragment of 400 voxels, considering only

Table 2. Reservoir properties of carbonates calculated from X-ray CT images

Sample	Porosity m (relative units)	Specific pore surface S_v (mm^{-1})	Permeability coefficient k_{NS} (μm^2)	Permeability coefficient of Carman k_{Carman} (μm^2)	Fractional deviation $d = 100 \cdot (k_{NS} - k_{Carman}) /$ k_{NS} (%)	Carman constant calculated using eq. (6)
Cb1	0.3	28.61	2.074	6.597	-218.1	15.83
Cb2	0.133	2.94	3.519	54.43	-1446.7	77.33
Cb3	0.093	2.12	0.504	35.79	-7001.2	355.1
Cb4	0.139	5.19	1.48	19.94	-1247.3	67.36
Cb5	0.289	11.14	11.32	38.9	-243.6	17.18
Cb6	0.106	1.93	384.49	63.94	83.4	0.83

**Figure 7.** Dependence of permeability coefficients on X-ray CT image size for sandstone Ss15 and carbonate Cb5.

matrix porosity. In this case variation in permeability at 25% was achieved, which is much lower than that in Table 2 and is comparable to sandstones in Table 1. The linear size of cubic REV for sample Cb5 corresponds to 150 voxels (or 2.76 mm), which is much higher than the similar parameter in sandstone.

Computational experiments have shown satisfactory comparability in sandstone permeability coefficients which are calculated on the basis of solutions of the Navier–Stokes and Kozeny–Carman equations.

It can be concluded that the Kozeny–Carman model is not suitable to evaluate the permeability of carbonate reservoirs with fracture porosity. However, Kozeny–Carman equation can describe the flow properties of carbonates with predominantly matrix porosity.

In the future, our research will include the evaluation of physical and chemical effects on porous media with different types of pore space genesis.

1. Barenblatt, G. I., Entov, V. M. and Ryzhik, V. M., *The Motion of Fluids and Gases in Natural Strata*, Nedra, Moscow, 1984, p. 207.
2. Nikolaevsky, V. N., *Geomechanics and Fluid Dynamics*, Nedra, Moscow, 1996, p. 448.
3. Romm, E. S., *Structural Models of the Pore Space of Rocks*, Nedra, Leningrad, 1985, p. 240.

4. Bulgakova, G. T., Sharifullin, A. R., Kharisov, R. Y., Baizigitova, A. V., Telin, A. G. and Pestrikov, A. V., Laboratory and technical studies of carbonate acid treatment. *Neftyanoe Khozyaystvo – Oil Industry*, 2010, **4**, 2–6.
5. Dvorkin, J. *et al.*, The future of rock physics: computational methods vs. lab. testing. *First Break*, 2008, **26**, 63–68.
6. Mostaghimi, P., Blunt, M. J. and Bijeljic, B., Computations of absolute permeability on micro-CT images. *Math. Geosci.*, 2013, **45**, 103–125.
7. Blunt, M. J. *et al.*, Pore-scale imaging and modeling. *Adv. Water Resour.*, 2013, **51**, 197–216.
8. Andrew, M., Bijeljic, B. and Blunt, M. J., Pore-scale contact angle measurements at reservoir conditions using X-ray tomography. *Adv. Water Resour.*, 2014, **68**, 24–31.
9. DeBoever, E., Varloteaux, C., Nader, F. H., Foubert, A., Békri, S., Youssef, S. and Rosenberg, E., Quantification and prediction of the 3D pore network evolution in carbonate reservoir rocks. *Oil Gas Sci. Technol.*, 2012, **67**, 63–68.
10. Wennberg, O. P., Rennan, L. and Basquet, R., Computed tomography scan imaging of natural open fractures in a porous rock; geometry and fluid flow. *Geophys. Prospect.*, 2009, **57**, 239–249.
11. Watanabe, N. *et al.*, X-ray CT based numerical analysis of fracture flow for core samples under various confining pressures. *Eng. Geol.*, 2011, **123**, 338–346.
12. Farber, L., Tardo, S. G. and Michaels, J. N., Use of X-ray tomography to study the porosity and morphology of granules. *Powder Technol.*, 2003, **132**, 57–63.
13. Mathews, P., Pone, J. N., Mitchell, J. D. and Halleck, P., High-resolution X-ray computed tomography observations of the thermal drying of lump-sized sub bituminous coal. *Fuel Process. Technol.*, 2011, **92**, 58–64.
14. Kuper, K. E. *et al.*, Three-dimensional distribution of minerals in diamondiferous eclogites, obtained by the method of high-resolution X-ray computed tomography. *Nucl. Instrum. Meth. Phys. Res. A*, 2007, **575**, 255–258.
15. Iassonov, P., Gebrenegus, T. and Tuller, M., Segmentation of X-ray computed tomography images of porous materials: a crucial step for characterization and quantitative analysis of pore structures. *Water Resour. Res.*, 2009, **45**, article number W09415.
16. Loitsyansky, L. G., *Fluid Mechanics*, Moscow, Nauka, 1973, p. 848.
17. Zakirov, T. R. and Nikiforov, A. I., Simulation of heat treating the oil collector using acid exposure on near-Wellbore zone. *Neftyanoe Khozyaystvo – Oil Industry*, 2014, **10**, 60–63.
18. Nikiforov, A. I., Zakirov, T. R. and Nikiforov, G. A., Model for treatment of oil reservoirs with polymer-dispersed systems. *Chem. Technol. Fuels Oils*, 2015, **51**, 105–112.
19. Zakirov, T. R., Nikiforov, A. I. and Latypov, A. I., Modeling thermal treatment in combination with acid treatment of a multi-layer oil reservoir. *Chem. Technol. Fuels Oils*, 2015, **50**, 449–452.
20. Roache, P. J., *Computational Fluid Dynamics*, Mir, Moscow, 1980, p. 608.

21. Belotserkovsky, O. M., Numerical modeling in continuum mechanics. *Phisico-matematicheskaya literatura*, 1994, p. 443.
22. Bear, J., *Dynamics of Fluids in Porous Media*, Elsevier, New York, 1972, p. 712.
23. Gosmen, A. D., Pan, V. M., Ranchel, A. K., Spalding, D. B. and Wolshtein, M., *Numerical Methods for the Viscous Liquid Flow Study*, Nedra, 1972, p. 324.
24. Saad, Y., Iterative methods for sparse linear systems. SIAM, 2003, p. 528.
25. Saad, Y., *Iterative Methods for Sparse Linear Systems*, Society for Industrial and Applied Mathematics, 2nd edn, 2003, p. 547.
26. <http://www.imperial.ac.uk/engineering/departments/earth-science/research/research-groups/perm/research/pore-scale-modelling/micro-ct-images-and-networks/>
27. Zhang, D., Zhang, R., Chen, S. and Soll, W. E., Pore scale study of flow in porous media: scale dependency, REV, statistical REV. *Geophys. Res. Lett.*, 2000, **27**, 1195–1198.
28. Al-Raoush, R. and Papadopoulos, A., Representative elementary volume analysis of porous media using X-ray computed tomography. *Powder Technol.*, 2010, **200**, 69–77.

ACKNOWLEDGEMENT. This work was funded by grant (RSCF) 15-11-10015.

Received 26 June 2015; revised accepted 16 December 2015

doi: 10.18520/cs/v110/i11/2142-2148

Variations in soil alter availability of carlinoside: an anti-hepatitic compound from *Cajanus cajan* (Linn.) leaves

Subhasish Das¹, Sandip Mukherjee²,
Rakesh Kundu², Pradip Bhattacharyya³,
Buddhadeb Duary⁴ and
Satya Sundar Bhattacharya^{1,*}

¹Department of Environmental Science, Tezpur University, Tezpur 784 028, India

²Department of Zoology, Visva Bharati, Santiniketan 731 235, India

³Indian Statistical Institute, North East Centre, Tezpur 784 028, India

⁴Palli Siksha Bhavana, Visva Bharati, Sriniketan 731 236, India

Agro-climatic factors largely regulate expression of phenolic compounds in plants. Carlinoside, a flavone glycoside, is known to eliminate bilirubin accumulation in rat liver. We cultivated *Cajanus cajan* uniformly in two different soil types – alluvial (AL) and laterite (LA). The climatic attributes and soil physico-chemical properties of the two localities were significantly different from each other. Carlinoside, phenol and flavonoid concentrations were higher in plants grown in AL than in LA soils. We recorded higher

UGT1A1 expression in liver hepatoma cell line HepG2 and rats treated with plant extracts from AL compared to LA.

Keywords: *Cajanus cajan*, carlinoside, plant phenolics, soil and climate.

CAJANUS CAJAN L. (Leguminosae) is an important legume crop extensively grown in India¹. The crop contributes significantly to the total pulse production of the country. However, apart from its high nutritive value, *C. cajan* leaf extract significantly heals alcohol-induced liver dysfunction in rats². The leaf extract contains a flavone glycoside, carlinoside that can convert insoluble bilirubin to soluble form³. The major problem in jaundice is the accumulation of free insoluble bilirubin, which is potentially toxic and may even cause death of the patient. In general, bilirubin–UGT enzyme (UGT1A1) converts insoluble bilirubin to a soluble innocuous form, which is eliminated through urine and faeces. Suppression of UGT1A1 enzyme by certain pathogens leads to the condition of jaundice, and no drug is available that can restore UGT1A1 activity^{2,3}.

The phenolic or polyphenol compounds account for approximately 40% of organic carbon circulating in the biosphere. Plants need these compounds for growth, reproduction, pigmentation and disease resistance. Several thousand phenols and polyphenols have been identified having a broad range of monomeric, dimeric and polymeric structures, amongst which 8150 or more are flavonoids and found in the epidermis of leaves and fruit skin of various plants⁴.

Climatic factors like solar radiation, temperature and humidity influence the concentration and quality of secondary metabolites in plants. Nutrient balance and solubility in soil is thought to play a major role in the production of secondary compounds in plants⁵. Various workers have documented considerable influence of environmental factors on the expression and concentration of bioactive compounds in plants⁶. Since plants cannot avoid environmental influence, nor can they migrate to regions with favourable habitat, they evolve highly complex mechanisms of adaptation. It has been demonstrated that expression of secondary metabolites is often altered due to these adaptive mechanisms⁷.

Carlinoside from the leaf extract of *C. cajan* is highly bioavailable and therefore has a potential in the treatment of jaundice³. However, expression and yield of carlinoside are expected to vary in different areas depending on specific agro-climatic conditions. This is the basic reason for non-uniform success of herbal medicine prepared from plants grown at different localities under varied environmental conditions. Since carlinoside concentration in the leaf is related to the site of growth of *C. cajan*, we conducted a study on the expression of total phenol, total flavonoids and carlinoside in *C. cajan* leaves collected

*For correspondence. (e-mail: satya72@tezu.ernet.in)